RSC Advances

PAPER

View Article Online
View Journal | View Issue

Cite this: *RSC Adv.*, 2026, **16**, 19079

$Na_2Cu_2TeO_6$: a potential material for high solar cell efficiency and superior energy-harvesting performance

Usma Shahzadi,[a] Muhammad Bin Javed,[a] Hafiz Tauqeer Ali,[b] Bassem F. Felemban[b] and S. Nazir *[a]

Materials having an antiferromagnetic (AFM) semiconducting ground state with a direct energy band gap (E_g) are attractive for photovoltaic (PV), energy-harvesting, and spintronic applications. In this work, numerous aspects of $Na_2Cu_2TeO_6$ (NCTO) are systematically investigated using first-principles calculations under biaxial ([110]) strain. The compound is found to be thermodynamically and mechanically stable. The unstrained phase exhibits a robust AFM ground state arising from strong superexchange coupling with a calculated local spin moment of $\sim 0.9\mu_B$ per Cu ion. The system possesses a direct E_g of 2.10 eV, with 100% accuracy compared to the experimental value. Under applied strain, the AFM ordering remains intact, while the E_g is tuned from 2.43 eV (−5%) to 1.81 eV (+5%) and retains its direct nature, leading to a pronounced enhancement of the PV rating. Notably, the spectroscopic limited maximum efficiency (SLME) increases from 20.47% in the unstrained case to a maximum value of 26.16% at +5% tensile strain, accompanied by a substantial rise in the short-circuit current density (J_{sc} = 19.01 mA cm^{-2}) and a high fill factor (FF ≈ 0.914). Furthermore, the electron effective mass (m^*) decreases from $\frac{m_e^*}{m_0} = 0.145$ to 0.131, while the hole m^* is reduced from $\frac{m_h^*}{m_0} = 0.616$ to 0.506 as the strain varies from −5% to +5%, indicating improved carrier mobility under tensile strain. Concurrently, the static dielectric constant exhibits a moderate increase from 3.76 to 3.89, leading to a reduction in the exciton binding energy (E_b) from 0.112 to 0.093 eV, which facilitates efficient charge separation. Additionally, thermoelectric analysis yields a high figure of merit of 0.81 at a −5% comparison at 1200 K, owing to an enhanced power factor and reduced lattice thermal conductivity. The Seebeck coefficient remains positive across all strain levels, indicating p-type conduction, while the electrical conductivity improves significantly under tensile strain. Collectively, these results demonstrate that biaxial strain is an effective route to simultaneously optimize the various physical features of the NCTO, establishing it as a promising multifunctional material for next-generation PV, energy-harvesting, and spin-dependent electronic devices.

Received 5th January 2026
Accepted 19th February 2026

DOI: 10.1039/d6ra00090h

rsc.li/rsc-advances

1 Introduction

A fundamental challenge in materials research lies in understanding the rich physics born from the delicate interplay of order and disorder. A highly promising group of materials are the double perovskites (DPOs) with the general formula $A_2BB'O_6$.[1,2] The A site is typically an alkaline or a rare-earth element, while the B and B′ sites are occupied by transition metals (TMs).[3] A key feature is that the B-site cations can arrange in an ordered or disordered octahedral pattern with oxygen,[4,5] and versatility originates from their tunable nature. The precise selection and combination of different cations at the distinct lattice sites allow for the direct design of targeted features like magnetism and electronic conductivity.[6] In particular, an interesting family within this group is the layered honeycomb oxides,[7] characterized by compositions $A_2M_2DO_6$ and $A_3M_2DO_6$, where A is an alkali/coinage metal (Li, Na, and K), M is a TM (Ni, Co, Zn, and Cu), and D is a chalcogen/pnictogen (Te, Sb, and Bi), which provide an ideal platform for studying how competing magnetic interactions (J_2/J_1 and J_3/J_1) stabilize new quantum states.[8] Ongoing research into specific compounds within this family highlight their diverse magnetic aspects. For instance, $Na_2Co_2TeO_6$ displays complex antiferromagnetic (AFM) ordering[9] and is a promising candidate for Kitaev spin-liquid behavior,[10,11] while $Na_3Ni_2SbO_6$

[a]*Department of Physics, University of Sargodha, 40100 Sargodha, Pakistan. E-mail: safdar.nazir@uos.edu.pk; Tel: +92-334-9719060*

[b]*Department of Mechanical Engineering, College of Engineering, Taif University, Kingdom of Saudi Arabia*

demonstrates the zigzag AFM state,[12] offering a further platform for studying magnetic frustration. Furthermore, in compounds like $Na_3LiFeSbO_6$, Na_4FeSbO_6, and Li_4MnSbO_6, the lack of long-range magnetic ordering is attributed to the effects of disorder and frustration.[13,14] An AFM state at low temperatures has also been observed in various O_3-type honeycomb compounds such as $Na_3M_2SbO_6$ (M = Cu, Ni), $Na_3Ni_2BiO_6$, and $Li_3Ni_2SbO_6$, alongside P2-type materials such as $Na_2M_2TeO_6$ (M = Co, Ni).[15–17] Likewise, $Na_2Cu_2TeO_6$ (NCTO) possesses a layered structure, where the Cu^{2+} ions form a distorted honeycomb lattice that is arranged in dimerized chains and directly shapes its magnetic behavior.[18]

In addition to their fascinating magnetic behavior, DPOs have gained attention for various optoelectronic (OE) and energy-conversion devices, attributed to their easily engineered electronic aspects and composition-dependent versatility.[3] For instance, in the realm of photovoltaics (PVs), lead-free DPOs like $Cs_2AgBiBr_6$ have been extensively investigated for their potential as stable and non-toxic light absorbers, where spectroscopic limited maximum efficiency (SLME) calculations predicting theoretical values exceeding 10%, showcase their promise for next-generation solar cells.[19] Similarly, DPOs such as Sr_2FeMoO_6 and Ba_2NiMoO_6 have demonstrated excellent photocatalytic activity, driven by their efficient charge separation and suitable E_g.[20,21] In the field of PV, the Ti-based halide double perovskite Cs_2TiBr_6 has attracted interest because of its optimal energy bandgap (E_g) of 1.8 eV, showing outstanding inherent stability, and a predicted SLME above 20%, positioning it among the most promising Pb-free absorber materials.[22] Furthermore, the TE performance of DPOs is a subject of growing interest, where a material like Sr_2TiCoO_6 is theoretically predicted to show a large Seebeck coefficient (S) owing to its complex electronic band structure, while its layered arrangement promotes phonon scattering and thus reduces lattice thermal conductivity (κ_L), an ideal combination for achieving a high figure of merit (ZT).[23] The $Rb_2LiAlTe_6$ DPO has emerged as a highly promising material, featuring an exceptionally low lattice thermal conductivity (κ_L < 0.5 W mK^{-1}) at room temperature and a predicted ZT > 1.5, largely due to its rattling ions and soft phonon modes.[24] More recently, halide DPOs like $Cs_2AgBiBr_6$ and $Cs_2AgBiCl_6$ have been synthesized and shown to possess an ultralow κ_L, a property paramount for efficient TE conversion, paving the way for their use in waste heat recovery applications.[25]

Moreover, the physical behavior of DPOs can be manipulated by adjusting their lattice parameters through various growth conditions, such as changes in temperature, hydrostatic pressure, depositing films on different substrates, and biaxial (biax.) strain. For example, Sr_2CoNbO_6 shows a rise in electrical resistivity and E_g under tensile (tens.) strain, while both features decrease, when compressive (comp.) strain is applied.[26] The Sr_2CrReO_6 structure shows a ferrimagnetic (FiM) to ferromagnetic (FM) transition when subjected to +2% biax. ([110]) or hydrostatic ([111]) strain.[27] Recently, Faiza-Rubab and Nazir, reported that the monoclinic $LaSr_{1-x}Ca_xNiReO_6$ DPO (for x = 0.0 and 0.5) undergoes an insulator–metal transition when subjected to −3% biax. comp. strain.[28] Subsequently, the effects of biax. ([110]) strain on Y_2NiIrO_6 is explored, revealing a half metal to insulator–metal transition at a critical −6% comp. strain, while +4%/+5% tens. strain induces FiM to FM/AFM magnetic transitions.[29] Likewise, applying −3% comp. strain to Sr_2CaOsO_6, triggers a transformation from semiconducting (SC) to half metal behavior.[30] Rout and Srinivasan, reported that applying −2.7% comp. strain transforms the C-type AFM insulating Bi_2FeReO_6 into a FiM half metal.[31] In addition, experimental studies indicate that when Re_2NiMnO_6 (Re = La, Pr, Nd, Sm, and Y) thin films are deposited on the $LaAlO_3$ substrates, a lattice mismatch arises. The resulting strain further distorts the $B(B')O_6$ octahedra, improving the magnetic aspects of the films and helping to maximize the T_C in DPO materials. Furthermore, strain-engineering is particularly powerful for optimizing functional aspects like PV efficiency and TE performance. For instance, in the field of PVs, biax. strain has been shown to directly tune the electronic band structure, a critical factor for light absorption.

For example, *ab initio* calculations demonstrate that strain tuned the E_g of the Janus C_{2h} Al_2XY (X/Y = S, Se and Te) monolayers from 2.25 to 2.57 eV, which enhances their potential from an OE and PV view point.[32] A prime example is the Pb-free halide $Cs_2AgBiBr_6$, where the application of +4% tens. strain was theoretically demonstrated to reduce indirect E_g from 1.95 to 1.65 eV, enhancing its overlap with the solar spectrum and potentially boosting its SLME.[33] Likewise, the OE features of Cs_2SnI_6 can be effectively engineered with strain. Theoretical predictions show that when applying +5% tens. strain, E_g increases to 1.48 eV from an unstrained value of 1.30 eV, while the material retains its efficient direct E_g structure. This precise control allows its properties to be optimized for the ideal Shockley–Queisser Limit, showcasing that strain is a powerful tool for material design.[34] As Guo *et al.* theoretically predicted that strain enhances the photocatalytic performance of the Janus Si_2PAs(SiXY) monolayers[35,36] and Ga_2SeTe/AlAs heterostructure,[37] as well as making them potential candidates for water splitting and solar cell applications. Similarly, strain methodology plays a pivotal role in enhancing TE aspects by decoupling electronic and thermal transport. A computational study on Ba_2ZnMoO_6 indicates that biax. strain aligns the electronic valleys within the conduction band, causing a substantial rise in the material's S and overall power factor (PF).[38]

Motivated by these prior results, we employed density functional theory (DFT) to systematically investigate the effect of biax. ([110]) strain on the numerous aspects of the newly synthesized NCTO DPO. A primary goal was to determine whether the AFM SC state remains stable under strain, which is a key question for both fundamental understanding and practical application. To thoroughly assess the material's potential, we extended our study to several traits, which are critical for real-world implementation. Also, we aimed to explore its OE performance by calculating optical features and estimating solar cell efficiency using the SLME method.[39] Finally, to evaluate its utility in thermal energy conversion, we planned a detailed computation of the TE transport coefficient, with particular focus on the ZT under varying strain conditions.[40]

This comprehensive approach was designed to establish whether NCTO is not only a compelling quantum magnetic material but also a viable candidate for next-generation energy-harvesting technologies.

2 Computational and structural details

Present calculations employed the full-potential linearized augmented plane-wave method as implemented in the WIEN2K code[41] within the framework of spin-polarized (SP) DFT.[42] For the exchange–correlation functional,[43] the Perdew–Burke–Ernzerchof[44] formulation of the generalized gradient approximation (GGA) is utilized.[45] Along with this, the correlation effects on the Cu 3d orbitals are taken into account with on-site coulomb interactions Hubbard parameter (U),[46] which varies from 4.0 to 7.0 eV to predict the correct electronic structure of the material. For the wave function expansion inside the atomic spheres, we set $l_{max} = 12$, while the plane-wave cutoff is set to $R_{mt} \times K_{max} = 6$ with $G_{max} = 24$. A k-mesh of $7 \times 8 \times 4$ having 300 points inside the irreducible wedge of the Brillouin zone is found to be well converged. Geometry optimization is performed until the atomic forces are less than 5 mRy per a.u. and total energy (E_t) convergence of less than 10^{-4} Ry is set for self-consistency.

NCTO crystallizes in a monoclinic structure having space group $C2/m$ (no. 12). The Na, Cu, Te, O1, and O2 ions occupy the Wyckoff positions of 4h, 4g, 2a, 8j, and 4i having experimentally observed atomic sites of (0, 0.1923, 0.5), (0, 0.6647, 0), (0, 0, 0), (0.1934, 0.1638, 0.1245), and (0.7562, 0, 0.1594), respectively. The experimental lattice parameters $a = 5.7024$ Å, $b = 8.6567$ Å, and $c = 5.9389$ Å with $\beta = 113.740°$ are used for the present study.[47] In its primitive unit cell, there are 4, 4, 2, and 12 atoms of Na, Cu, Te, and O, respectively. The crystal structure of the NCTO, presented in Fig. 1, reveals a framework that is built from one-dimensional chains of CuO_6 octahedra. These chains are linked by Te atoms in a distorted tetrahedral symmetry. The structure is stabilized by Na ions residing in the interstitial sites, which ensure charge balance, while the characteristic inclination of the unit cell axis clearly reflects its monoclinic symmetry.

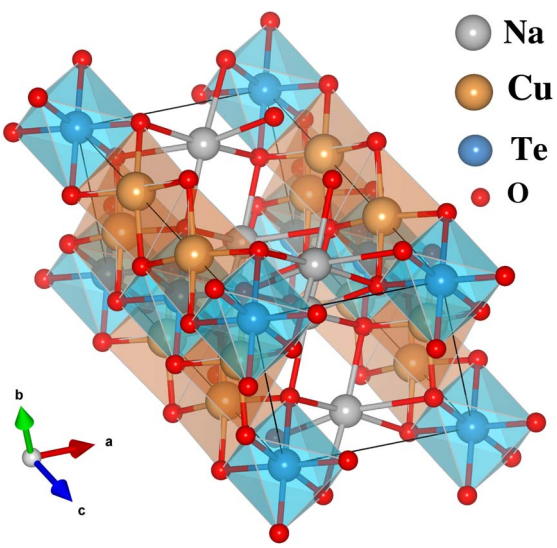

Fig. 1 Schematic representation of the $Na_2Cu_2TeO_6$ structure.

3 Results and discussion

3.1 Unstrained system

First, we began by evaluating the structural stability of the unstrained NCTO material using formation enthalpy (ΔH_f) calculations:[27]

$$\Delta H_f = \frac{1}{22}\left[E_t^{Na_4Cu_4Te_2O_{12}} - 4E_t^{Na} - 4E_t^{Cu} - 2E_t^{Te} - 12E_t^{O}\right] \quad (1)$$

where 22 is the total number of atoms and $E_t^{Na_4Cu_4Te_2O_{12}}$ represent the E_t of the primitive cell of the NCTO motif. Similarly, E_t^{Na}, E_t^{Cu}, E_t^{Te}, and E_t^{O} are the per-atom E_t in the most stable low-temperature phases of the Na, Cu, Te, and O atoms, correspondingly. The estimated ΔH_f is plotted against various U values in Fig. 2(a), which are negative and range from −0.9693 to −0.7831 eV per atom across the entire U levels. The consistently negative ΔH_f indicates that the formation process is exothermic, which means that the energy is released when the constituent elements combine to form a compound. This thermodynamic favorability suggests that the material is inherently stable.

Next, the magnetic ground state (MGS) of the unstrained structure was identified by comparing the E_t of the FM and AFM

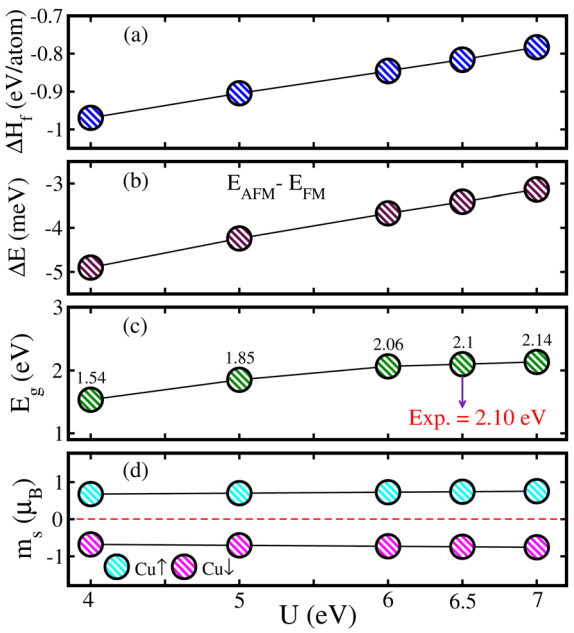

Fig. 2 GGA+U calculated: (a) formation enthalpy (ΔH_f), (b) energy differences between antiferromagnetic (AFM) and ferromagnetic (FM) states ($\Delta E = E_{AFM} - E_{FM}$), (c) energy band gap ($E_g$), and (d) local spin magnetic moments (m_s) on the Cu atoms as a function of the Hubbard (U) parameter, which varies from 4.0 to 7.0 eV on the Cu 3d state in the $Na_2Cu_2TeO_6$ structure.

spin-ordering (SO). In the FM SO, spins of both Cu ions are aligned parallel (↑↑) having a large net moment. On the other hand, the spin on one Cu atom is oriented opposite to each other (↑↓), leading to the perfect AFM state with a zero net moment. Thus, we evaluated the MGS of the system by computing the energy difference ($\Delta E = E_{AFM} - E_{FM}$) from its AFM and FM phases across the various U values as shown in Fig. 2(b). The negative sign of ΔE at each U level indicates that AFM SO is more stable than that of the FM one, which aligns well with the experimental results.[47] This implies that the anti-parallel alignment between Cu ions (both in-plane and out-of-plane orientations) is favorable. Subsequently, the electronic structure of the system in its stable AFM state was analyzed by computing E_g against numerous U values on the Cu 3d state as depicted in Fig. 2(c). The E_g increases from 1.54 to 2.14 eV as U is raised from 4.5 eV to 7.0 eV and at a critical U level of 6.5 eV, the computed E_g of 2.10 eV is in excellent agreement with the experimentally observed value of 2.10 eV (ref. 47) having 100% accuracy. For a qualitative analysis of the electronic structure of the NCTO material, the computed SP total density of states (TDOS) for various U levels on the Cu 3d state is presented in Fig. 1S of the SI. The conduction band edge shifts substantially away from the Fermi level (E_F), increasing the E_g magnitude (see Fig. 1S(a–c) of the SI). For $U = 6.5$ eV on the Cu 3d state, E_g of 2.10 eV is obtained, converging closely with the experimental value of 2.10 eV (see Fig. 1S(d) of the SI). Therefore, for further investigations, we fixed the U of 6.5 eV on the Cu 3d state.

A deeper understanding of the electronic contributions near the E_F is achieved through SP partial density of states (PDOS) of the Te 2p, Cu 3d, and O 2p states that are plotted in Fig. 3(a). The PDOS reveals the distinct roles of various orbitals in shaping the electronic structure of the NCTO. The valence band region, extending from approximately −5 eV up to E_F, is predominantly constituted by Cu 3d and O 2p states with a significant degree of hybridization between them. This strong Cu 3d and O 2p orbitals mixing indicates covalent bonding character within the CuO_6 octahedra, which is crucial for the structural stability and electronic features of the material. Specifically, the states closest to the valence band maximum (VBM) are primarily composed of Cu 3d character. In contrast, the conduction band is mainly formed by the Cu 3d state. In addition, the calculated SP band structure for the stable AFM SO in Fig. 3(b) further corroborates the semiconducting behavior of the material. A well-defined direct E_g of 2.10 eV exists between the VBM and CBM that lies on the same Γ symmetry point (see Fig. 3(b)), which is crucial for OE applications where a direct and tunable E_g is desirable.

Finally, the system magnetism was probed by plotting the partial spin magnetic moment (m_s) on both Cu ions in the stable AFM state of the unstrained NCTO against U in Fig. 2(d). The calculated m_s of $0.9\mu_B$, confirms the oxidation state of +2 of the Cu ion, which almost remains constant as U increases. Moreover, m_s on the Cu1 and Cu2 ions show "+" and "−" sign, affirming the AFM SO as well. For further insight into the origin of system magnetism, the 3D spin-density isosurfaces owing to an iso-value of 0.05 e Å^{-3} for the stable AFM SO of the NCTO material is plotted in Fig. 4. The highly localized spin densities around Cu sites confirm their role as the sole magnetic carriers. As the Cu^{2+} ($3d^9$) ion is in an octahedral crystal field, it results in $t_{2g}^3\uparrow\ t_{2g}^3\downarrow\ e_g^2\uparrow\ e_g^1\downarrow$ electron distribution leaving a single unpaired electron in its e_g orbitals. This is visualized as a distinct e_g orbital lobe geometry in the isosurface. Crucially, the spin-densities on the two Cu sites (Cu1 and Cu2) are of identical magnitude but display opposite colors (pink and blue), confirming the AFM coupling between them as well (see Fig. 4). Alongside, the robust anti-parallel alignment in the NCTO

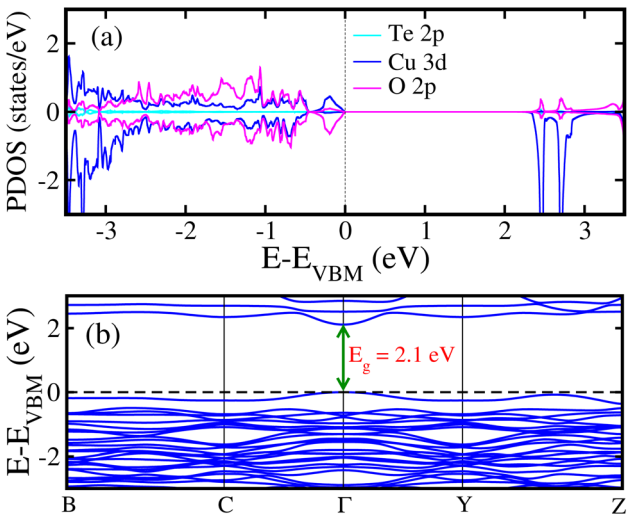

Fig. 3 GGA+U (U = 6.5 eV on the Cu 3d state) calculated spin polarized: (a) partial density of state (PDOS) on the Te 2p/Cu 3d/O 2p orbitals and (b) band structure (only for one spin channel) for the $Na_2Cu_2TeO_6$ material in the stable antiferromagnetic state.

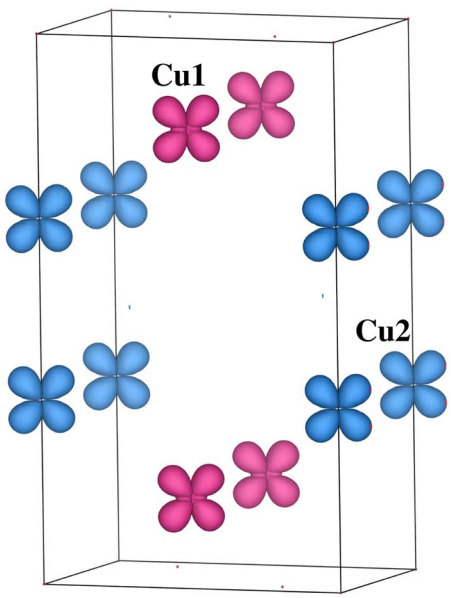

Fig. 4 Computed 3D spin-magnetization density isosurfaces for the $Na_2Cu_2TeO_6$ material in the stable antiferromagnetic spin state. For clarity, Na, Te, and O ions are omitted.

material is visualized by a superexchange interaction between the adjacent Cu1 and Cu2 ions as presented in Fig. 5. The AFM coupling is operated by virtual electron hopping *via* oxygen (O^{2-}). The nearly 180° Cu–O–Cu bond angle in the NCTO, provides an ideal geometry for this strong and direct super-exchange pathway, maximizing the overlap between the Cu $d_{x^2-y^2}$ (e_g) and O 2p orbitals. The mechanism is governed by the electronic configuration of the Cu^{2+} ($3d^9$) ions, which possess a single unpaired electron in the e_g orbitals. The unpaired e_g electron from one Cu ion in the spin up (↑) state can virtually hop onto the oxygen, because the oxygen 2p orbital hosts a spin-down (↓) electron, which validates the Pauli-exclusion principle. This electron can in turn hop virtually onto the neighboring Cu ion, which possesses a spin-down e_g state partially empty to receive it. This two-step virtual process results in a net lowering of the system's energy, when the spins on the two Cu ions are anti-parallel, thereby stabilizing the AFM ground state. Hence, the specific path and strength of this interaction as depicted schematically in Fig. 5, are crucial to understanding the magnetic aspects of the materials.

3.2 Strained system

Now, to evaluate the strain-dependent behavior of the NCTO DPO, we performed a comprehensive analysis under biax. strain along the *ab*-plane ([110]), varying the experimental lattice constants from −5% to +5%. Here, "−" and "+" signs represent the comp. and tens. levels, correspondingly. Here, it should be noted that the atoms are allowed to relax in all directions, which means atomic position optimization is taken into account for all strained structures. Initially, the thermodynamic stability of the system under strain is quantified by computing ΔH_f as depicted in Fig. 2S of the SI. The determined ΔH_f values remain negative across the entire strain range, confirming that all the strained configurations are thermally stable and can be synthesized under normal conditions. However, the stability is enhanced under tens. strain as evidenced by the more negative ΔH_f values, while comp. strain results in comparatively less negative ΔH_f, indicating reduced structural stability than that of the unstrained one. Furthermore, the material's mechanical stability was evaluated by calculating the elastic stiffness tensors (C_{ij}) under three strain conditions (−5%, 0%, and +5%), which is done through the application of six finite deformations and analysis of standard stress–strain relations.[48,49] Therefore, 13 individual C_{ij} are estimated for the monoclinic phase of the NCTO material across the three measured strain levels, which are listed in Table 1. The majority of C_{ij} values are positive and meet the necessary and sufficient Born stability criteria as:[50]

$$C_{11}>0,\quad C_{22}>0,\quad C_{33}>0,\quad C_{44}>0,\quad C_{55}>0,\quad C_{66}>0$$
$$C_{33}C_{55}-C_{35}^{2}>0,\quad C_{44}C_{66}-C_{46}^{2}>0,\quad C_{22}+C_{33}-2C_{23}>0$$
$$C_{22}\left(C_{33}C_{55}-C_{35}^{2}\right)+2C_{23}C_{25}C_{35}-C_{23}^{2}C_{55}-C_{25}^{2}C_{33}>0$$
$$2(C_{15}C_{25})(C_{33}C_{12}-C_{13}C_{23})+C_{15}C_{35}(C_{22}C_{13}-C_{12}C_{23})+C_{25}C_{35}(C_{11}C_{23}-C_{12}C_{13})-h+C_{55}g>0$$

where

$$g=C_{11}C_{22}C_{33}-C_{11}C_{23}^{2}+2C_{23}C_{25}C_{35}-C_{23}^{2}C_{55}-C_{25}^{2}C_{33}>0$$

$$h=C_{15}^{2}(C_{22}C_{33}-C_{23}^{2})+C_{25}^{2}(C_{11}C_{33}-C_{13}^{2})+C_{35}^{2}(C_{11}C_{22}-C_{12}^{2})>0$$

Moreover, a systematic comparison of the derived elastic moduli Young's modulus (Y), shear modulus (G), and bulk modulus (B) was conducted for each strain level as illustrated in Fig. 6. The B is a measure of a material's resistance to uniform volumetric compression and exhibits exceptional stability across the strain conditions. The calculated values revealed a clear decreasing trend in the B amplitude with applied strain, falling from 151.75 GPa at −5% to 82.75 GPa at +5% strain. This consistent decline indicates a progressive loss of resistance to volumetric compression and a significant softening of the material's structure. Similarly, Y is also known as the elastic modulus and is a measure of a material's stiffness. A high value implies that the material strongly resists deformation under stress, while a low value characterizes a more flexible and easily shaped substance. It decreases from 191.57 GPa at −5% strain to 157.27 GPa at 0% and finally to 126.1 GPa at +5%. Along with this, G which is the ratio of shear stress to strain and indicates a material's resistance to shape deformation, fell from 74.28 GPa (−5%) to 61.13 GPa (0%) and further to 50.61 GPa (+5%).

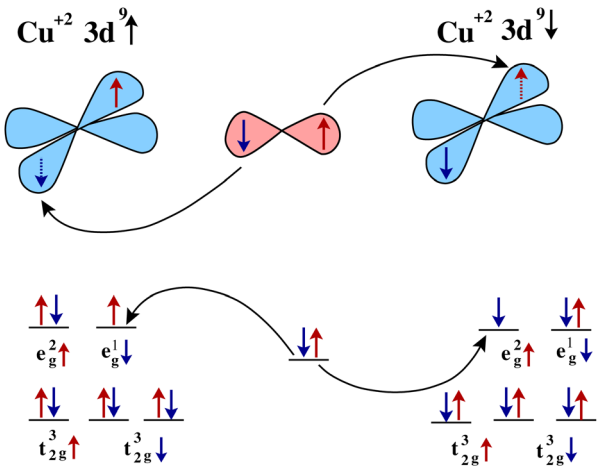

Fig. 5 Superexchange mechanism between Cu1 and Cu2 3d orbitals *via* oxygen 2p state by mediating feasible Cu^{2+}–O^{2-}–Cu^{2+} ($e_g^1\uparrow$–$2p^2$–$e_g^1\downarrow$) coupling in the $Na_2Cu_2TeO_6$ material.

Table 1 Computed 13 independent elastic constants (C_{ij}) of the $Na_2Cu_2TeO_6$ material under −5%, 0%, and +5% biaxial ([110]) strains

Strain	C_{11}	C_{12}	C_{13}	C_{15}	C_{22}	C_{23}	C_{25}	C_{33}	C_{35}	C_{44}	C_{46}	C_{55}	C_{66}
−5%	219.42	87.09	81.11	0.19	213.69	147.01	0.36	349.94	0.06	75.86	0.12	85.11	67.44
0%	174.08	48.48	48.04	−1.08	167.51	95.92	−0.87	282.55	−1.08	57.49	0.14	67.42	47.01
+5%	136.97	33.91	34.25	−0.04	135.09	64.31	0.15	239.36	−0.05	45.57	0.06	56.78	36.69

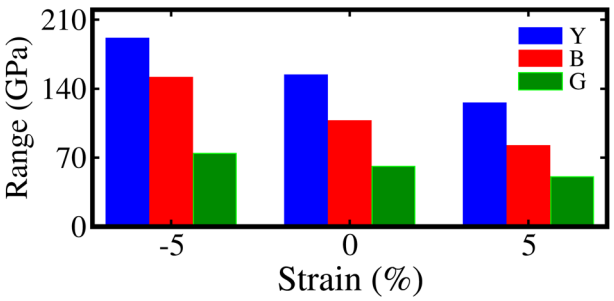

Fig. 6 Computed bulk modulus (B), Young's modulus (Y), and shear modulus (G) of the $Na_2Cu_2TeO_6$ material under −5%/0%/+5% strain.

Additionally, to determine the ductile, brittle, and bonding nature of the compounds, we computed the Pugh's ratio $\left(\frac{B}{G}\right)$, Poisson's ratio (ν), $\frac{G}{B}$, and Cauchy's pressure (C_p) as displayed in Fig. 3S of the SI. The materials are classified as brittle if their $\frac{B}{G}$ ratio is <1.75 and ductile if it is >1.75. Hence, our computed values of $\frac{B}{G}$ are 2.04/1.76/1.64 under −5%/0%/+5% strain (see Fig. 3S(a) of the SI), which indicate a ductile-to-brittle transition with the material being ductile at −5% and 0% strain but brittle at +5% strain. Next, the bonding character can be determined using the $\frac{G}{B}$ ratio and ν, where approximately 0.65/0.25 points to ionic bonding and near 1.1/0.1 signifies covalent bonding. Consequently, the computed values of the $\frac{G}{B}$ ratio/ν are 0.489/0.289, 0.566/0.262, and 0.612/0.246 at strains of −5%, 0%, and +5%, respectively, consistent with a material exhibiting ionic bonding (see Fig. 3S(b) and (c) of the SI). Moreover, C_p indicates the nature of bonding and ductility in a material. A positive C_p suggests metallic/ductile bonding, while a negative C_p points to covalent/brittle bonding. Thus, under +5% strain, C_p is negative, confirming covalent/brittle character. In contrast, at strain and under −5% strain, it shows positive values, which align with metallic/ductile bonding. Here, it is worth mentioning that the material reveals a ductile-to-brittle transition at approximately +5% tens. strain, as indicated by the Pugh's ratio analysis. For practical application in flexible PV, this transition is not a limiting factor but a valuable design parameter. The operational strain in most flexible PV devices, involving bending on conformal surfaces, typically remains below 2–3%, well within the ductile regime identified here. The clear transition point at +5% strain provides a predictable and well-defined upper limit for mechanical failure, which is crucial for ensuring long-term device reliability and establishing safety factors in engineering designs. Furthermore, this strain tolerance represents a significant advancement over conventional brittle PV materials, underscoring the potential of this compound for use in next-generation, durable flexible electronics.

Along with this, to analyze the strain-dependent elastic behavior of the NTCO material, we calculated its elastic anisotropy using ElATools, specifically assessing the three-dimensional anisotropic features under −5%, 0%, and +5% strain. The changes in the 3D anisotropic features Y, ν, linear compressibility (β), and G are shown in Fig. 7(a)–(d), respectively. Table 2 lists their extreme values and associated

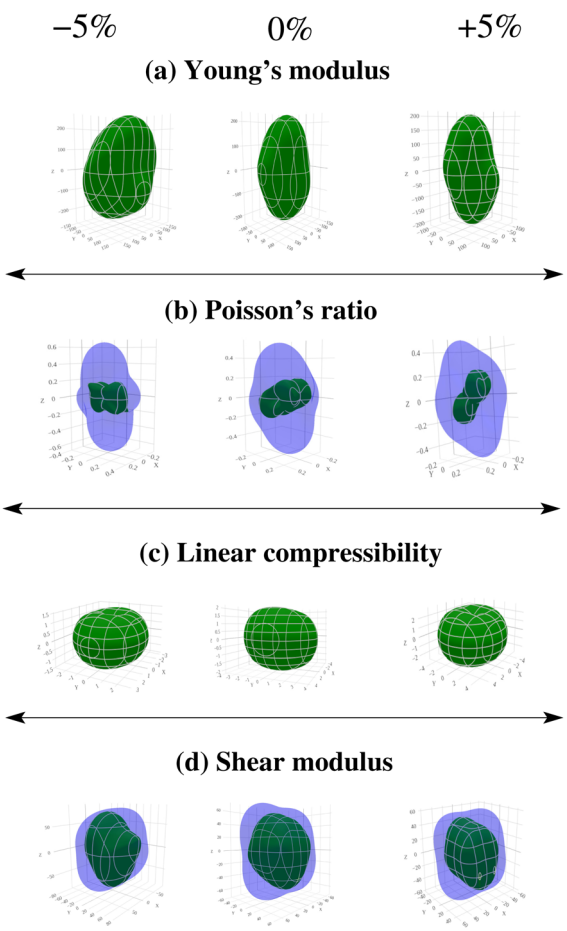

Fig. 7 Three-dimensional directionally dependent: (a) Young's modulus, (b) Poisson's ratio, (c) linear compressibility, (d) shear modulus of the $Na_2Cu_2TeO_6$ material under −5% (left column)/0% (middle column)/+5% (right column) strain.

Table 2 Computed numerous elastic features of the $Na_2Cu_2TeO_6$ material under −5%, 0%, and +5% biaxial ([110]) strain

	Young's modulus			Linear compressibility			Shear modulus			Poisson's ratio		
Strain	Y_{min}	Y_{max}	A	β_{min}	β_{max}	A	G_{min}	G_{max}	A	ν_{min}	ν_{max}	A
−5%	133.98	267.27	1.995	0.991	3.108	3.138	55.817	96.122	1.722	0.082	0.658	8.567
0%	119.27	225.89	1.894	1.495	4.28	2.863	46.376	84.322	1.818	0.065	0.557	8.567
+5%	93.181	206.55	2.217	2.018	5.569	2.759	34.031	72.173	2.121	0.021	0.513	24.368

anisotropic factors. As illustrated in Fig. 7(a), Y exhibits significant directional hardening under both tens. and comp. levels. Notably, it expands substantially under the −5% condition, indicating enhanced stiffness along specific crystallographic axes. In contrast, ν as shown in Fig. 7(b), demonstrates a relatively stable directionally sensitive response, with its values varying distinctly from the reference state under −5% strain. Furthermore, the behavior of β, depicted in Fig. 7(c), undergoes a notable transition. While it retains an approximately isotropic, spherical character under −5% strain, it evolves into a highly anisotropic shape with elongated lobes along particular directions under 0% and +5% strain. This suggests a strain-induced loss of isotropic symmetry. Finally, G, presented in Fig. 7(d), displays pronounced anisotropy with directional variations up to ±5% from the unstrained reference, an effect that is most critical under the −5% comp. strain. Collectively, these results underscore the profound influence of external strain on the anisotropic elastic response of NCTO.

To determine the effect of strain on the MGS, we computed $\Delta E = E_{AFM} - E_{FM}$ against strain, which is plotted in Fig. 8(a). The persistent negative values of ΔE across both comp. and tens. strain levels, confirms that the AFM remains the MGS of the NCTO material as determined in the unstrained situation. This robustness highlights the system's strong preference for AFM SO, which remains undisturbed by lattice deformations for the considered feasible strain range. Next, the influence of strain on the electronic aspects of the NCTO was examined in its AFM MGS. To do this, first we plotted the determined E_g against strain in Fig. 8(b), which increases from 2.17 to 2.43 eV under the comp. strain of −1% to −5% and decreases from 1.88 to 1.81 eV for tens. strain of +1% to +5%. This continuous tunability of the E_g, highlights the effectiveness of strain as a control parameter for modulating the electronic features of the system.

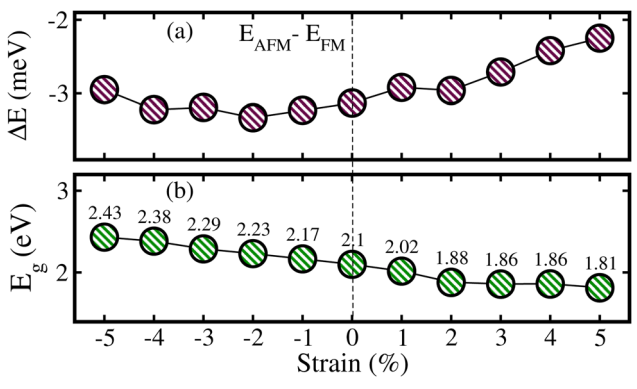

Fig. 8 GGA+U calculated: (a) energy differences between antiferromagnetic (AFM) and ferromagnetic (FM) states ($\Delta E = E_{AFM} - E_{FM}$) and (b) energy band gap (E_g) in the $Na_2Cu_2TeO_6$ material against ±5% biaxial ([110]) strain.

For a qualitative study, we present the SP TDOS of the NCTO DPO under comp. (left column) and tens. (right column) strain ranging from 1% to 5% in Fig. 4S(a)–(e) and Fig. 4S(a′)–(e′) of the SI, respectively. Under comp. strain of −1% to −5%, the TDOS reveals a progressive widening of the energy separation between the VBM and CBM. Specifically, the leading edge of the valence band shifts to lower energies (further left), while the conduction band edge shifts to higher energies (further right). This symmetric pulling apart of the band edges, driven by increased orbital overlap and bandwidth, directly corresponds to the rising E_g from 2.17 eV to 2.43 eV. Conversely, under tens. strain from +1% to +5%, the VB and CB come closer, narrowing the E_g from 2.02 to 1.81 eV. Further, to validate the TDOS results, the band structures of the NCTO under various comp. and tens. strains are plotted in Fig. 9. Direct inspection of the band structure validates the TDOS findings, offering a detailed picture of how the VBM and CBM evolve at high symmetry points under strain. Critically, the fundamental nature of the E_g remains direct across the entire range of applied comp. of −1% to −5% (see Fig. 9(a)–(c)) and tens. strain of +1% to +5% (see Fig. 9(a′)–(c′)). The strain only modulates the magnitude of the E_g without inducing a direct-to-indirect transition. This further enhances its potential for PV/OE applications due to its stable direct nature.

Next, the carrier transport behavior of NCTO was examined through a systematic evaluation of electron and hole effective mass (m^*) under biax. ([110]) strain ranging from −5% to +5%. The m^*, a critical descriptor of carrier mobility, was extracted from the curvature of the CB and VB edges at the Brillouin zone center. To quantify this curvature, the near-Γ energy dispersion was locally approximated using a quadratic polynomial, enabling direct determination of m^* *via* the second-order energy-momentum relationship as:

$$m^* = \hbar^2 \left(\frac{d^2 E}{dk^2} \right)^{-1} \quad (2)$$

here, $\hbar$, E, and k represent the reduced Planck's constant, energy, and wave vector, respectively. All values are reported relative to the free-electron mass for consistency. As illustrated in Fig. 10(a), the electron $\frac{m^*}{m_0}$ remains comparatively low and

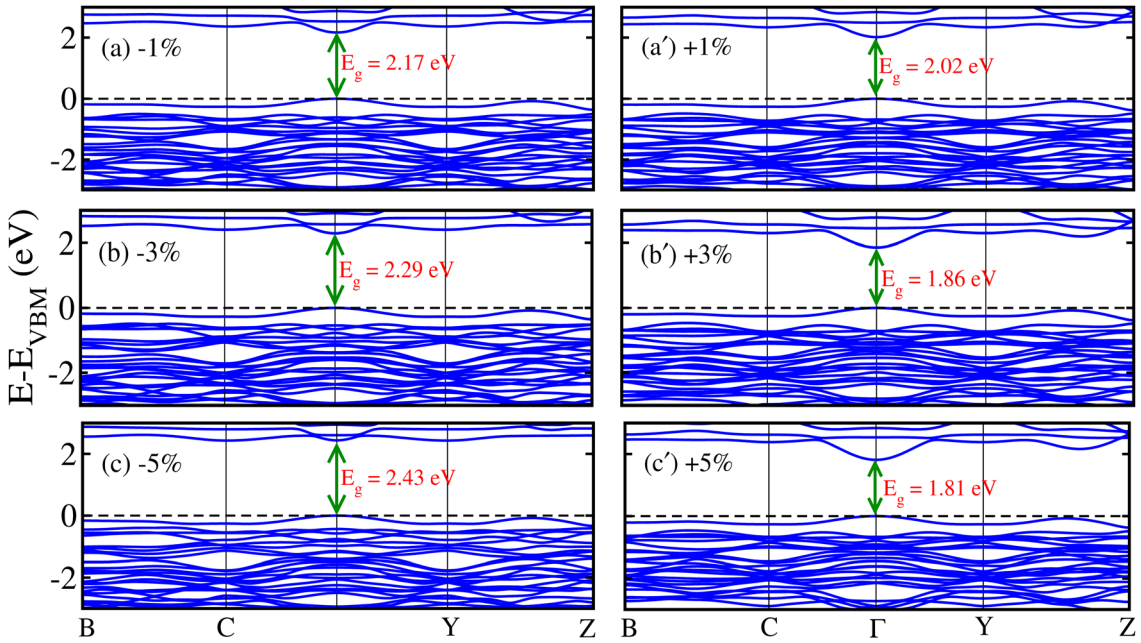

Fig. 9 GGA+U calculated band structures under biaxial ([110]) compressive/tensile (−/+) strain for the: (a and a′) 1%, (b and b′) 3%, and (c and c′) 5% levels of the $Na_2Cu_2TeO_6$ material.

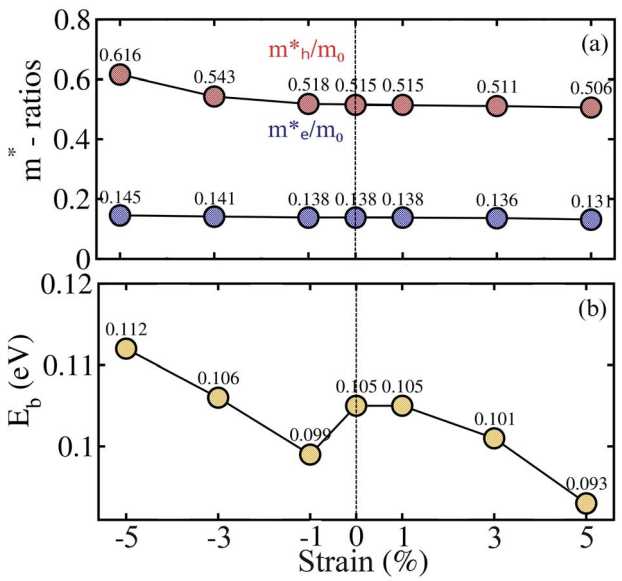

Fig. 10 (a) Calculated (a) effective mass (m^*) ratio of holes $\left(\frac{m_h^*}{m_0}\right)$/electrons $\left(\frac{m_e^*}{m_0}\right)$ in red/blue color and (b) variation of the exciton binding energy (E_b) in the $Na_2Cu_2TeO_6$ structure against −5% to +5% biaxial ([110]) strain.

exhibits a mild decreasing trend with increasing tens. strain, reducing from 0.145 at −5% to 0.131 at +5%. In contrast, holes $\left(\frac{m_h}{m_0}\right)$ are significantly heavier, though their m^* gradually decreases from 0.616 to 0.506 across the same strain interval. This pronounced asymmetry between electron and hole masses suggest electron-dominated transport in strained NCTO, which is advantageous for OE applications. In parallel, the excitonic response was analyzed by estimating the exciton E_b, which reflects the coulombic attraction within electron–hole pairs and is modeled using the relation:[51]

$$E_b = 13.56 \frac{m_\mu}{m_0} \frac{1}{\varepsilon_1^2(0)} \quad (3)$$

where $\varepsilon_1(0)$ denotes the static constant and m_0 is the reduced m^*. As shown in Fig. 10(b), E_b displays a clear strain-dependent modulation, attaining its maximum value of 0.112 eV under −5% comp. strain and progressively declining to 0.093 eV at +5% tens. strain. This reduction in E_b under tens. deformation implies weaker electron–hole binding, which can facilitate exciton dissociation and improve free-carrier generation efficiency. Moreover, the reduction of the exciton E_b from 0.112 to 0.093 eV under tens. strain significantly enhances charge-separation efficiency, positioning the material among the best perovskite absorbers. This value approaches that of optimized lead-halide perovskites such as $FAPbI_3$ (0.01–0.02 eV),[52] which is lower than inorganic $CsPbI_3$ (0.02–0.05 eV).[53] It is also dramatically smaller than lead-free double perovskites such as $Cs_2AgBiBr_6$ (0.4–0.5 eV)[54] and layered PEA_2PbI_4 (0.2–0.3 eV),[53] highlighting its strong potential for PV applications. Collectively, the coexistence of low electron m^* and moderate, strain-tunable exciton E_b underscores the promise of NCTO as a mechanically adaptable material for PV and OE devices. In addition, to assess the strain dependence of magnetic aspects, the Cu m_s variations in the NCTO system against strain are discussed in Fig. 5S of the SI. The m_s values remain almost constant to $\pm$ 0.8μ_B across the entire strain range from −5% to +5%. This remarkable consistency confirms the preservation of the Cu^{2+} oxidation state under lattice deformation.

Furthermore, the maintained opposite signs of m_s on the Cu1 (↑) and Cu2 (↓) sublattices, affirm that the AFM SO remains dominant under both comp. and tens. strain conditions, demonstrating the robustness of the system magnetism against structural modifications.

The investigation of DPOs specifically that contain direct E_g, which interestingly lies in the visible spectrum region, has emerged as a prominent candidate in the field of solar cells, OE, PVs, light-emitting diodes (LEDs), and radiation detectors.[3,55,56] Therefore, the ability to engineer their electronic structure through chemical substitution and external stimuli like strain, makes them a fascinating class of materials for advanced optical devices. Key optical parameters, such as the dielectric function ($\varepsilon(\omega)$) and the absorption coefficient ($\alpha(\omega)$), provide deep insight into a material's light–matter interactions and electronic transition behavior. The complex $\varepsilon(\omega)$ is expressed as $\varepsilon(\omega) = \varepsilon_1(\omega) + i\varepsilon_2(\omega)$,[57] where $\varepsilon_1(\omega)$ and $\varepsilon_2(\omega)$ represent the real and imaginary components, respectively. The $\varepsilon_1(\omega)$ relates to the material's refractive characteristics, while the $\varepsilon_2(\omega)$ accounts for absorption due to interband electronic transitions. Other optical features such as reflectivity, refractive index, and energy loss can be derived from $\varepsilon(\omega)$. Therefore, in this study we only focus on the plots of $\varepsilon_1(\omega)$, $\varepsilon_2(\omega)$, and $\alpha(\omega)$ for the unstrained and under tens. strain as shown in Fig. 11(a)–(c). Here, $\varepsilon_1(\omega)$ obtained *via* the Kramers–Krong[58] relation, reveals the electronic polarizability. At zero photon energy, the static $\varepsilon(\varepsilon(0))$ is a key parameter influencing charge carrier recombination rates and device efficiency. A higher $\varepsilon(0)$, generally reduces carrier recombination thereby enhancing device performance. The energy-dependent $\varepsilon_1(\omega)$ for 0%/1%/3%/5% tens. strain is graphically presented in Fig. 11(a). The calculated $\varepsilon_1(\omega)$ for 0%/1% is 3.75, while it increases to 3.80/3.89 for 3%/5% tens. strain. As the photon energy increases $\varepsilon_1(\omega)$ fluctuates and attains a peak value of 5.1/5.0/4.9/5.0 at 3.7/3.6/3.4/3.3 eV for 0%/1%/3%/5% tens. strain. Afterwords, $\varepsilon_1(\omega)$ falls with some oscillations and minimizes at 2.1/2.2/2.2/2.1 at 4.9/4.9/4.7/4.5 eV for 0%/1%/3%/5% tens. strain indicating that light is now being absorbed more than it is polarizing the material.

Moreover, $\varepsilon_2(\omega)$, is directly linked to the electronic structure and optical absorption. The absorption edge, corresponding to the fundamental E_g, appears at 0.02 eV for 0%/1%/3%/5% tens. strain, indicating a transition between the VB and CB near high-symmetry points, as presented in Fig. 11(b). A sharp rise in $\varepsilon_2(\omega)$ is observed once the photon energy exceeds the E_g, signifying the onset of VB to CB transitions. Strong absorption peaks appear in the ultraviolet (UV) region, with the first prominent peak located at 4.7 eV for the unstrained NCTO material, shifting to 4.6/4.5/4.2 eV under 1%/3%/5% tens. strain (see Fig. 11(b)). These shifts are attributed to strain-induced changes in the lattice parameters and E_g tuning. Both tens. and comp. strains induce blue or red shifts in the $\varepsilon_2(\omega)$ spectra, enabling tunable absorption for targeted applications. Now we consider $\alpha(\omega)$, which describes the penetration depth of light in the material before absorption, a critical parameter for PVs and photodetectors. It is calculated using the relation:[59]

$$\alpha(\omega) = \frac{\sqrt{2}\omega}{c}\left[\sqrt{\varepsilon_1{}^2(\omega) + \varepsilon_2{}^2(\omega)} - \varepsilon_1(\omega)\right]^{1/2} \quad (4)$$

and the onset of $\alpha(\omega)$ is found to follow a trend similar to $\varepsilon_2(\omega)$. The unstrained and tens.-strained systems exhibit strong absorption within the 3–6 eV range. Maximum absorption values of 0%/1%/3%/5% tens. strain are achieved at 4.8/4.7/4.6/4.4 eV (see Fig. 11(c)). Hence, enhanced absorption in the visible region under tens. strain suggests improved performance in the solar cells and visible-light photodetectors.

Likewise, we present the calculated $\varepsilon_1(\omega)/\varepsilon_2(\omega)/\alpha(\omega)$ for −1%/−3%/−5% comp. strain in Fig. 6S(a)–(c) of the SI. The $\varepsilon_1(\omega)$ initiates from 3.8 at 0.02 eV for all −1%/−3%/−5% comp. strains. It almost remains constant from 0.02–0.06 eV, then it fluctuates and attains a maximum value of 5.1/5.2/5.3 at 3.7/3.8/3.9 eV for −1%/−3%/−5% comp. strain (see Fig. 6S(a) of the SI), respectively. The peak signifies a resonance condition, indicating maximum electronic polarizability and the strongest light–matter interaction at that specific energy. Beyond this, $\varepsilon_1(\omega)$ exhibits subsequent variations suggesting the complex interplay of multiple electronic interband transitions occurring at higher energies. Furthermore, the $\varepsilon_2(\omega)$ spectrum reveals a notable redistribution of spectral weight and a shift in the critical peaks under −1%/−3%/−5% comp. strain. The first prominent peak, corresponding to the direct optical transition from the VB to the CB, is located at 4.0/4.2/4.3 eV for −1%/−3%/−5% comp. strain (see Fig. 6S(b) of the SI). This systematic shift signifies a direct modulation of the electronic band structure, where comp. strain blue-shifts the peak while tens. strain

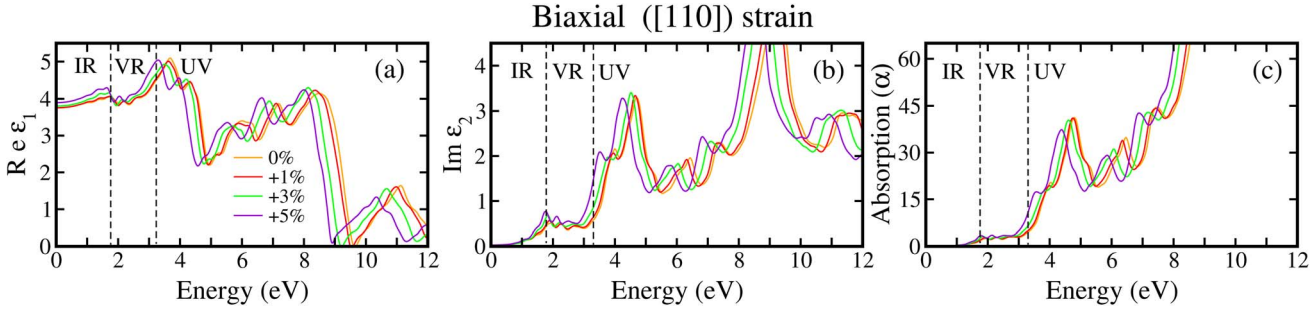

Fig. 11 Calculated optical parameters: (a) real dielectric part ($\varepsilon_1(\omega)$), (b) imaginary dielectric part ($\varepsilon_2(\omega)$), and (c) absorption coefficient ($\alpha(\omega)$) in 10^4 cm^{-1} under 0%/1%/3%/5% biaxial ([110]) strain for the $Na_2Cu_2TeO_6$ material.

induces a red-shift, thereby demonstrating a tunable optical response. A similar trend is also observed in $\alpha(\omega)$, where the peak values for −1%/−3%/−5% comp. strain are 41/40/38 cm^{-1} at 4.8/4.9/4.9 eV as shown in Fig. 6S(c) of the SI. The pronounced and tunable absorption in the visible-to-UV range, suggests that NCTO DPO is an excellent candidate for LEDs and laser diodes. The strain-engineered E_g allows for precise control over the emitted wavelength, which is critical for high color rendering solid-state lighting and targeted laser applications.[60] Hence, a significant $\alpha(\omega)$ makes it a suitable material for non-linear optical devices and as an active gain medium in waveguide-based photonic circuits.[61]

Next, the PV potential of the NCTO motif oxide was evaluated using the SLME metric following the methodology established by Yu and Zunger.[62] This approach provides a realistic assessment of PV performance by accounting for both absorptivity and recombination losses. The SLME was computed against strains to systematically investigate the strain-dependent PV response. The SLME is defined as the ratio of maximum extractable power to incident solar power:

$$\eta = \frac{P_{max}}{P_{in}} \tag{5}$$

where P_{in} represents the incident solar power density (AM1.5G spectrum, 100 mW cm^{-2}). The maximum power density P_{max} is derived from the current density–voltage characteristics:

$$P_{max} = \max\left[\left(J_{sc} - J_0\left(\exp\left(\frac{eV}{k_B T}\right) - 1\right)\right)V\right] \tag{6}$$

with J_{sc} as the short-circuit current density, J_0 as the reverse saturation current density, V as the voltage, e as the electron charge, k_B as Boltzmann's constant, and $T = 300$ K. The short-circuit current is computed from the absorptivity $A(E)$:

$$J_{sc} = e\int_0^\infty A(E) I_{sun}(E) dE \tag{7}$$

and the radiative recombination current density is given by:

$$J_0^r = \frac{e}{\pi}\int_0^\infty A(E) I_{bb}(E, T) dE \tag{8}$$

where $I_{sun}(E)$ and $I_{bb}(E, T)$ represent the AM1.5G solar spectrum and blackbody radiation spectrum, respectively. For NCTO, which exhibits a direct E_g, the radiative recombination fraction $f_r = 1$, indicates that only radiative recombination mechanisms are considered.

Table 3 Photovoltaic parameters of the $Na_2Cu_2TeO_6$ material under biaxial strain at optimal thickness of 11.514 μm

Strain (%)	SLME (%)	J_{sc} (mA cm^{-2})	J_0 (A cm^{-2})	V_{oc} (V)	FF
−5	14.05	7.29	1.52×10^{-37}	2.064	0.933
−3	16.59	9.21	2.63×10^{-35}	1.937	0.930
−1	20.47	12.59	3.50×10^{-32}	1.759	0.924
+0	20.47	12.59	3.50×10^{-32}	1.759	0.924
+1	22.19	14.31	7.62×10^{-31}	1.683	0.921
+3	25.57	18.25	3.57×10^{-28}	1.530	0.915
+5	26.16	19.01	9.92×10^{-28}	1.505	0.914

The calculated PV parameters under various strain conditions are summarized in Table 3 and also illustrated in Fig. 12. A pronounced strain-dependent evolution of SLME is observed with efficiency increasing monotonically from 14.05% at −5% compressive strain to 26.16% at +5% tens. strain. This represents an 86% relative enhancement from maximum compressive to maximum tens. strain, highlighting the significant tunability of PV performance through strain engineering in NCTO. The efficiency enhancement under tens. strain arises from a complex interplay between competing PV parameters. As strain increases from −5% to +5%, J_{sc} exhibits substantial improvement from 7.29 to 19.01 mA cm^{-2}, representing a 2.6-fold increase. This enhancement in photocurrent generation stems from favorable modifications to the electronic band structure under tens. strain, which improves optical absorption characteristics. Conversely, the V_{oc} shows a monotonic decrease from 2.064 V at −5% strain to 1.505 V at +5% strain, reflecting the reduction in E_g under tens. deformation. The J_0 increases by approximately nine orders of magnitude across the strain range, indicating enhanced recombination rates at higher tens. strains. The fill factor (FF), calculated as:

$$FF = \frac{P_{max}}{V_{oc} \times J_{sc}} \tag{9}$$

remains consistently high (0.914–0.933) across all strain conditions, with a slight decreasing trend under tens. strain. Despite the reduction in V_{oc} and fillfactor (FF), the substantial enhancement in J_{sc} dominates the overall efficiency improvement, resulting in net performance gains.

Fig. 12(a) presents the thickness-dependent SLME for NCTO under various strain conditions, revealing that optimal performance is achieved at approximately 11.5 μm for all strain states. This represents a significantly reduced optimal thickness compared to many conventional PV materials, offering potential advantages for material utilization and device fabrication. The thickness dependence of individual PV parameters (FF, V_{oc}, J_{sc}, and J_0) is shown in Fig. 12(c)–(f), illustrating the fundamental trade-offs in PV optimization. The strain-dependent SLME trend shown in Fig. 12(b), demonstrates a near-linear relationship between tens. strain and efficiency enhancement, with the highest efficiency of 26.16%. This performance surpasses many emerging PV materials and approaches the practical efficiency limits for single-junction solar cells. The asymmetric response to comp. *versus* tens. strain reveals that NCTO is particularly responsive to tens. deformation with comp. strain inducing more severe performance degradation relative to the unstrained baseline. The convergence of optimal thickness around 11.5 μm across the strain range, coupled with the substantial efficiency enhancement under tens. strain, positions strained NCTO as a promising candidate for flexible PV applications where strain engineering can be readily implemented. The demonstrated efficiency of 26.16% at +5% tens. strain, achieved with a relatively thin absorber layer, suggests that NCTO-based solar cells could offer competitive performance with reduced material consumption. So, this comprehensive analysis establishes biax. strain as a powerful tuning parameter for optimizing the PV performance of NCTO,

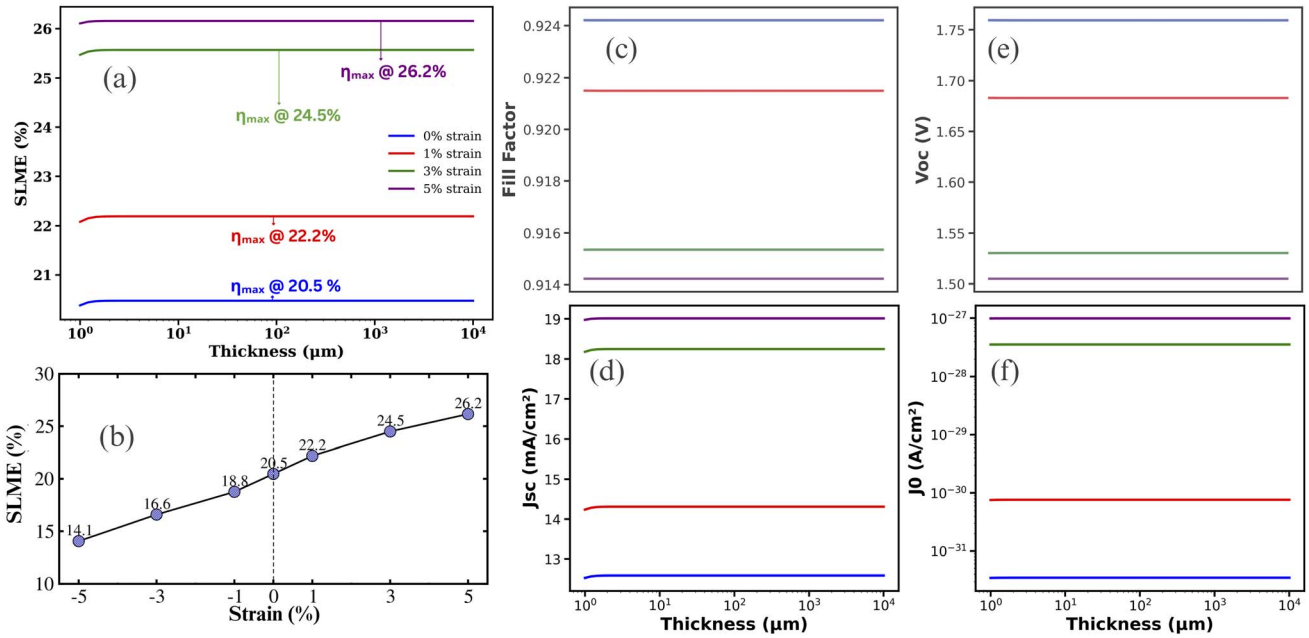

Fig. 12 (a and b) Calculated spectroscopic limited maximum efficiency (SLME) as a function of thickness/strain at the optimal thickness of 11.514 μm, (c) fill factor (FF), (d) short-circuit current density (J_{sc}), (e) open-circuit voltage (V_{oc}), and (f) reverse saturation current density (J_0), *versus* thickness of the $Na_2Cu_2TeO_6$ structure.

with tens. strain particularly effective for enhancing light absorption and overall device efficiency, while maintaining favorable charge-extraction features. Moreover, almost all the strained structures keep the optimal thickness of 11.514 μm, which has practical advantages as compared to other materials.

Now, TE behavior of the system is analyzed as DPOs have gained importance in the last decade due to their ability to address the worldwide energy crisis.[63] These materials are used in smart sensors, energy harvesting, and the emerging field of thermo-power wave source,[64] as TE power generators serve as effective green energy sources, by directly converting thermal energy into electrical energy.[65] In this fashion, it has been established that DPOs have recently gained considerable attention and become a preferred choice for advanced TE applications due to their outstanding traits[66] and utility in a diverse array of applications. These include solid-state refrigeration,[67] advanced heating and cooling systems,[68] solar thermal energy conversion,[69] thermal management of laser diode,[70] and energy harvesting.[71] The fascinating potential of DPOs as TE materials is directly attributable to a specific set of physical aspects such as electrical conductivity (σ) per relaxation time $\left(\frac{\sigma}{\tau}\right)$, S, PF per relaxation time $\left(\mathrm{PF} = \frac{S^2\sigma}{\tau}\right)$, susceptibility ($\chi$), conductivity ($\kappa$), and $ZT = \frac{\sigma S^2 T}{\kappa}$. Thus, the transport aspects are investigated by applying semi-classical Boltzmann theory, a method executed using the BoltzTraP code,[72] integrated with the Wien2K program. The calculated TE parameters near the E_F – $\frac{\sigma}{\tau}$, S, PF, χ, κ, and dimensionless ZT – for the unstrained and strained NCTO DPO as a function of temperature, ranging from 100 to 1200 K, are plotted in Fig. 13(a)–(f), respectively.

For many semiconducting materials, τ lies between 10^{-13} and 10^{-14} seconds indicating the flow of electric charge, which is essential for transporting significant power through a material subjected to a temperature gradient.[73,74] Hence, for the analysis of TE aspects, a constant τ of 10^{-14} seconds was adopted. Fig. 13(a) reveals a consistent increase in $\frac{\sigma}{\tau}$ from 0.032/0.082/0.079 $\times$ 10^{19} Ω^{-1} m^{-1} s^{-1} 100 K to 0.65/0.72/0.70 $\times$ 10^{19} Ω^{-1} m^{-1} s^{-1} at 1200 K under −5%/0%/+5% strain, correspondingly. Electrical resistivity (ρ) decreases as $\frac{\sigma}{\tau}$ increases with temperature, which results in greater charge carrier conduction. Among the unstrained (0%) and the strained conditions, +5% tens. level yields the highest values, suggesting a significant enhancement in charge carrier mobility relative to −5% comp. strain. Next, S is also an important TE factor for determining the electronic aspects, which measures the TE voltage produced across the two ends of a conductor in response to temperature gradient (ΔT), which is expressed as$S = \frac{\Delta V}{\Delta T}$.[75,76] Fig. 13(b) displays the temperature-dependent behavior of S across −5%/0%/+5% biax. strain. At 0%/+5%, S initiates from approximately 1.99/2.08 $\times$ 10^{-4} μV K^{-1} at 100 K and increases with temperature reaching a peak value of around 2.06/2.09 $\times$ 10^{-4} μV K^{-1} at 300 K before declining to about 1.55/1.57 $\times$ 10^{-4} μV K^{-1} at 1200 K. In contrast, the −5% comp. strain condition suppresses the S at higher temperature, beginning at a significantly high value of 2.77 $\times$ 10^{-4} μV K^{-1} at 100 K and gradually decreasing with rising temperature, achieving a minimum value of 1.75 $\times$ 10^{-4} μV K^{-1} at 1200 K. The positive

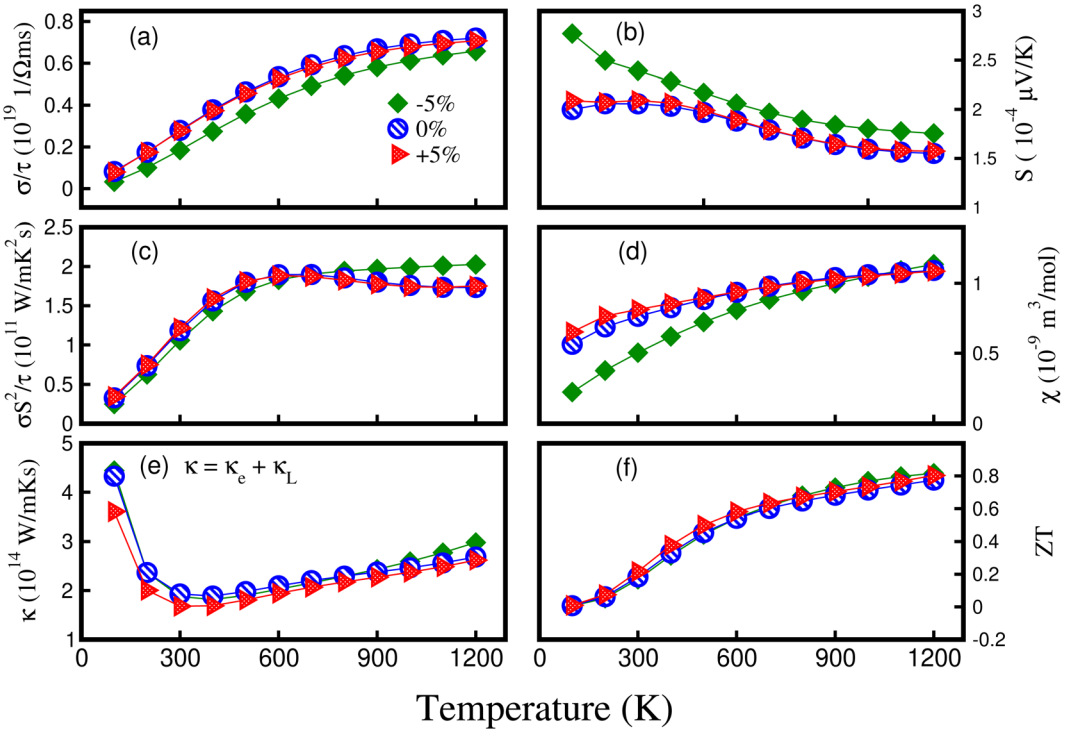

Fig. 13 Computed various thermoelectric features of the $Na_2Cu_2TeO_6$ structure under −5%/0%/+5% strain.

sign of S across all conditions confirms p-type conduction. This demonstrates that strain engineering, particularly comp. strain, is an effective strategy for enhancing the TE potential of this material by optimizing the S over a specific temperature range. Another crucial TE parameter is PF, which is a combined effect of S^2 and $\frac{\sigma}{\tau}$, serving as a critical quantity for evaluating a material's TE conversion efficiency as shown in Fig. 13(c). For −5% comp. strain, PF exhibits a consistent monotonic increase over the entire temperature range, which starts from 0.25×10^{11} W mK^{-2} s^{-1} at 100 K and rises steadily to a value of 2.03×10^{11} W mK^{-2} s^{-1} at 1200 K. However, PF shows a non-linear trend with temperature under 0%/+5% strain. Initially, it increases and reaches a peak of $1.89/1.88 \times 10^{11}$ W mK^{-2} s^{-1} at 700/600 K and then experiences a significant drop, ending near $1.73/1.75 \times 10^{11}$ W mK^{-2} s^{-1} at 1200 K for 0%/+5% strain. This illustrates that comp. strain provides the most stable and improving performance, making it superior for applications over a wide temperature range.

Now, χ, describes the response of a TE material to variations in external conditions such as electric or magnetic fields. It enhances with rising temperature, which is $0.23/0.56/0.65 \times 10^{-9}$ m^3 mol^{-1} at 100 K to $1.14/1.09/1.08 \times 10^{-9}$ m^3 mol^{-1} at 1200 K under 0%/+5% strain as presented in Fig. 13(d). Afterward, we discuss κ, which measures the heat conduction contributed by charge carriers and is a fundamental parameter in the analysis of TE phenomena. The total κ is equal to $\kappa_e + \kappa_L$, where the electronic contribution (κ_e) comes from charge carriers (electrons and holes) and the κ_L comes from phonons. The κ_e was determined directly from the electronic transport aspects. However, to obtain the κ_L, we employed the Slack model,[77] which requires key mechanical parameters as inputs. First, the longitudinal (v_l) and transverse (v_t) sound velocities were computed using the formula:[78,79]

$$v_l = \left(\frac{3B + 4G}{3\rho}\right)^{\frac{1}{2}} \tag{10}$$

$$v_t = \left(\frac{G}{\rho}\right)^{1/2}$$

these were then used to calculate the average sound velocity ($v_{avg.}$) as:

$$v_{avg.} = \left[\frac{1}{3}\left(\frac{2}{{v_t}^3} + \frac{1}{{v_l}^3}\right)\right]^{-\frac{1}{3}}.$$

Subsequently, the Debye temperature (Θ_D), which is critical for the Slack model calculation of κ_L, was derived as:[80]

$$\Theta_D = \frac{h}{k_B}\left[\frac{3n}{4\pi}\left(\frac{N_A\rho}{M}\right)\right]^{1/3} v_{avg.} \tag{11}$$

where h, N_A, k_B, M, n, and ρ are Plank's constants, Avogadro's number, Boltzmann's constant, molecular mass, number of atoms in the unit cell, and density, respectively, whereas the term $v_{avg.}$ is average sound velocity. Thus, the κ_L in the Slack model is calculated as:[77]

$$\kappa_L = \frac{A{\Theta_D}^3 V^{1/3} M_{avg.}}{v^2 n^{2/3} T} \tag{12}$$

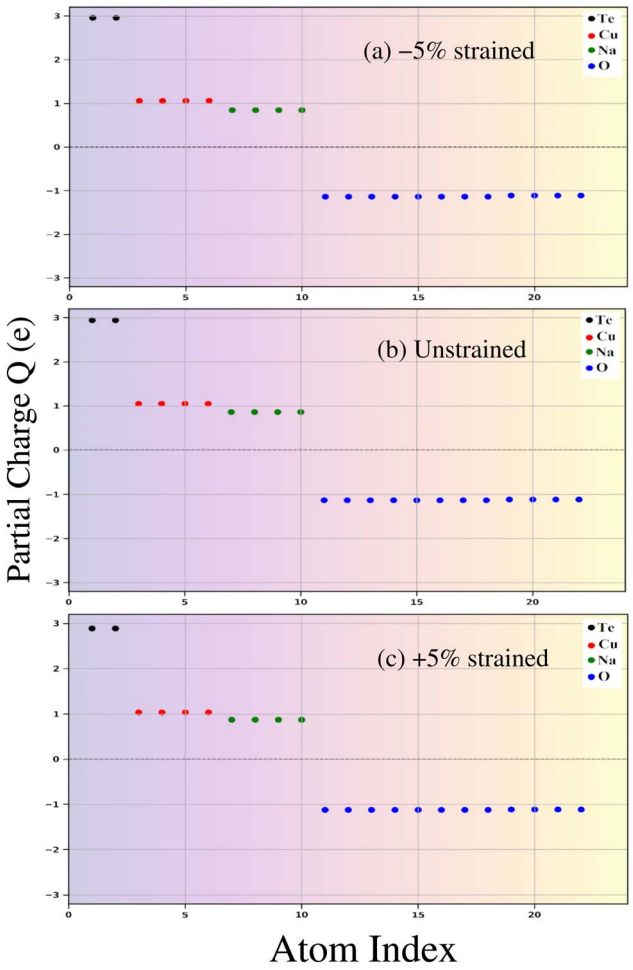

Fig. 14 Bader charge analysis of the $Na_2Cu_2TeO_6$ material for: (a) −5%, (b) unstrained and (c) +5% doping levels.

here, $M_{avg.}$ = average molar mass per atom, V = volume per atom, and T = temperature in kelvin, and A = constant that depends on γ (γ = Grüneisen parameter), which further depends on ν, expressed as:[81]

$$\gamma = \frac{3(1+\nu)}{2(2-3\nu)} \tag{13}$$

$$A(\gamma) = \frac{2.43 \times 10^{-8}}{\left[1 - \left(\frac{0.514}{\gamma}\right) + \left(\frac{0.228}{\gamma^2}\right)\right]}. \tag{14}$$

The resulting temperature dependent $\kappa = \kappa_e + \kappa_L$ is plotted in Fig. 13(e) under −5%/0%/+5% strain. At the beginning, κ decreases to a minimum value of 1.81/1.88/1.68 × 10^{14} W mK^{-1} s^{-1} at 400 K, followed by a steady increase and reaches a peak of 2.98/2.68/2.61 × 10^{14} W mK^{-1} s^{-1} at 1200 K across −5%/0%/+5%. Due to overall low κ, this material is ideal for waste heat harvesting solutions. Lastly, we computed ZT:[82]

$$ZT = \frac{\sigma S^2 T}{\kappa} \tag{15}$$

as the performance of TE materials can be predicted by their ZT and materials with large values of about unity or greater than unity are considered highly potential candidates for TE devices. Fig. 13(f) shows the graph of ZT with temperature for −5%/0%/+5%, which shows approximately the same behavior under all strain conditions. It is clear from the figure that ZT increases over the entire temperature range, which starts from a low value of 0.006/0.008/0.009 at 100 K and rises consistently to a high value of about 0.81/0.77/0.80 at 1200 K for −5%/0%/+5% strain level. This superb performance is a direct consequence of the optimally balanced electronic features (a high and stable PF as seen in Fig. 13(c)) combined with the significantly suppressed κ (see Fig. 13(e)). Hence, the strain engineering, successfully decouples electronic and thermal transport, pushing the ZT value closer to unity and marking a major step towards viable TE applications. Basically, the physical mechanism behind the strained modulated physical features of the system is that strain tuned the chemical bonding (bond lengths and bond angles) among the ions, which further optimizes atomic orbital hybridization. Thus, these changes regulate the electronic, magnetic, optical, and thermoelectric properties of the motif.

Ultimately, the Bader charge assessment is considered to analyze the charge transfer among ions, which substantially modulate the physical behavior of the system for unstrained and strained structures. It is revealed that the Na/Cu/Te/O ions contain average partial charges of approximately +0.848/+1.055/+2.958/−1.127e under −5% strain (see Fig. 14(a)). For the unstrained and +5% strained NCTO motif, the calculated partial charges on the Na/Cu/Te/O ions are +0.862/+1.049/+2.943/−1.128e, and +0.874/+1.038/+2.888/−1.118e (see Fig. 14(b) and (c)), respectively. These consistent charge values across different strain levels (−5%, 0%, and +5%) indicate a stable charge distribution. The positive charges on the Na, Cu, and Te confirm their role as charge donors, while the negative charge on oxygen establishes it as the charge acceptor. Charge is systematically transferred from the cations to the oxygen anions, supporting an ionic character in bonding. The stability of the Bader charges across all applied strains suggests that the electronic structure remains robust, with no significant charge redistribution induced by mechanical deformation. This resilience highlights the material's potential for applications where structural strain does not severely compromise charge transport or bonding integrity.

4 Conclusion

To summarize, first-principles calculations were employed to investigate the thermodynamic, mechanical, electronic, magnetic, optical, solar-cell efficiency, and thermoelectric (TE) features of the newly synthesized $Na_2Cu_2TeO_6$ material in its unstrained as well as biaxial ([110]) strained forms. The results indicate that the structures are thermodynamically and mechanically stable in all considered cases. The unstrained system displays an antiferromagnetic (AFM) semiconducting ground state, which is preserved under the full strain range and is attributed to strong AFM superexchange coupling between partially filled high-energy Cu1 $e_g^1\uparrow$ and Cu2 $e_g^1\downarrow$ orbitals. The

computed partial spin moment on the Cu ion is $\sim 0.9\mu_B$, corresponding to a $3d^9$ electronic configuration ($t_{2g}^3\uparrow\, t_{2g}^3\downarrow\, e_g^2\uparrow\, e_g^1\downarrow$) with a spin value of $S = 0.5$. Moreover, optical analysis of the frequency-dependent dielectric function ($\varepsilon(\omega)$) and absorption coefficient ($\alpha(\omega)$) confirms that the material exhibits strong optical activity across the whole spectrum range under both unstrained and strained conditions. Strain engineering induces a tunable direct energy band gap (E_g), which narrows from the compressive to tensile regime and leads to a pronounced enhancement in PV performance. Notably, the system exhibits a very high spectroscopic limited maximum efficiency (SLME) of 26% at +5% tensile strain, where the E_g reduces to 1.81 eV. This enhancement is accompanied by an increase in short-circuit current density and a high fill factor, despite a moderate reduction in the open-circuit voltage, highlighting the effectiveness of strain for optimizing solar-cell-relevant parameters. In addition, strain favors tailoring the carrier transport and excitonic properties. As tensile strain reduces the electron and hole effective mass from $\frac{m_e^*}{m_0}/\frac{m_h^*}{m_0} = 0.145/0.616$ at -5% strain to 0.131/0.506 at +5% strain, indicating improved carrier mobility. Concurrently, the static dielectric constant exhibits a moderate increase, which leads to a systematic reduction in the exciton E_b from 0.112 to 0.093 eV across the same strain range, facilitating efficient charge separation and further supporting the enhanced photovoltaic (PV) response. Furthermore, TE evaluations performed from 100 to 1200 K reveal a dominant p-type transport behavior, characterized by a positive Seebeck coefficient, and a significantly enhanced figure of merit of 0.81 at -5% compressive strain due to reduced lattice thermal conductivity. Overall, the coexistence of a robust AFM ground state, direct E_g, high SLME, strain-enhanced carrier transport, reduced exciton E_b, and near-unity *ZT* value establishes NCTO as a highly promising multifunctional material for spintronic, PV, and TE transport applications.

Conflicts of interest

The authors declare no competing interests.

Data availability

The data that support the findings of this study are available from the corresponding author upon reasonable request.

Supplementary information (SI) is available. See DOI: https://doi.org/10.1039/d6ra00090h.

Acknowledgements

The authors would like to acknowledge the Deanship of Graduate Studies and Scientific Research, Taif University, for funding this work.

Notes and references

1 A. Grimaud, K. J. May, C. E. Carlton, Y.-L. Lee, M. Risch, W. T. Hong, J. Zhou and Y. Shao-Horn, *Nat. Commun.*, 2013, **4**, 2439.
2 M. Shaikh, A. Fathima, M. Swamynadhan, H. Das and S. Ghosh, *Chem. Mater.*, 2021, **33**, 1594–1606.
3 M. G. Basavarajappa and S. Chakraborty, *ACS Mater. Au*, 2022, **2**, 655–664.
4 J. A. Abraham, D. Behera, K. Kumari, A. Srivastava, R. Sharma and S. K. Mukherjee, *Chem. Phys. Lett.*, 2022, **806**, 139987.
5 C. Agarwal, H. Mittal, T. Bano, J. Kumar, M. Gora, A. Kumar, S. Chandra, S. Vikal, Y. K. Gautam and S. Kumar, *Indian J. Pure Appl. Phys.*, 2022, **10**, 1–16.
6 H. A. Evans, L. Mao, R. Seshadri and A. K. Cheetham, *Annu. Rev. Mater. Res.*, 2021, **51**, 351–380.
7 U. F. Seifert and M. Vojta, *Phys. Rev. B*, 2019, **99**, 155156.
8 G. M. Kanyolo, T. Masese, A. Alshehabi and Z.-D. Huang, *Mater. Today Chem.*, 2023, **33**, 101657.
9 W. Yao, K. Iida, K. Kamazawa and Y. Li, *Phys. Rev. Lett.*, 2022, **129**, 147202.
10 L. Balents, *Nature*, 2010, **464**, 199–208.
11 A. Kitaev, *Ann. Phys.*, 2006, **321**, 2–111.
12 P.-F. Wang, H.-R. Yao, Y. You, Y.-G. Sun, Y.-X. Yin and Y.-G. Guo, *Nano Res.*, 2018, **11**, 3258–3271.
13 W. Schmidt, R. Berthelot, L. Etienne, A. Wattiaux and M. A. Subramanian, *Mater. Res. Bull.*, 2014, **50**, 292–296.
14 N. Bhardwaj, A. Gupta and S. Uma, *Dalton Trans.*, 2014, **43**, 12050–12057.
15 R. Berthelot, W. Schmidt, A. Sleight and M. Subramanian, *J. Solid State Chem.*, 2012, **196**, 225–231.
16 W. Schmidt, R. Berthelot, A. Sleight and M. Subramanian, *J. Solid State Chem.*, 2013, **201**, 178–185.
17 L. Viciu, Q. Huang, E. Morosan, H. Zandbergen, N. Greenbaum, T. McQueen and R. Cava, *J. Solid State Chem.*, 2007, **180**, 1060–1067.
18 S. Gao, L.-F. Lin, A. F. May, B. K. Rai, Q. Zhang, E. Dagotto, A. D. Christianson and M. B. Stone, *Phys. Rev. B*, 2020, **102**, 220402.
19 F. Hao, C. C. Stoumpos, D. H. Cao, R. P. Chang and M. G. Kanatzidis, *Nat. Photon.*, 2014, **8**, 489–494.
20 X. Y. Li, Z. F. Yao, L. Y. Zhang, G. H. Zheng, Z. X. Dai and K. Y. Chen, *Appl. Surf. Sci.*, 2019, **480**, 262–275.
21 S. Bazrafshan, J. He and S. S. Naghavi, *J. Phys. Chem. C*, 2023, **127**, 3968–3976.
22 M. A. Islam and R. Paul, *Opt. Quantum Electron.*, 2023, **55**, 957.
23 P. Roy, I. Bose and T. Maiti, *Integr. Ferroelectr.*, 2016, **174**, 34–42.
24 S.-N. Hsu, W. Zhao, Y. Gao, Akriti, M. Segovia, X. Xu, B. W. Boudouris and L. Dou, *Nano Lett.*, 2021, **21**, 7839–7844.
25 F. Elfatouaki, O. Farkad, R. Takassa, S. Hassine, O. Choukri, A. Ouahdani, E. Ibnouelghazi, D. Abouelaoualim and A. Outzourhit, *Sol. Energy*, 2023, **260**, 1–10.

26 A. Kumar, R. Shukla, A. Pandey, S. Dalal, M. Miryala, K. Ueno, M. Murakami and R. Dhaka, *J. Appl. Phys.*, 2020, **128**, 025303.
27 Q.-U. Ain, S. Naseem and S. Nazir, *Sci. Rep.*, 2020, **10**, 13778.
28 S. Faiza-Rubab and S. Nazir, *Phys. Chem. Chem. Phys.*, 2022, **24**, 17174–17184.
29 U. Saeed, A. Islam, B. F. Felemban, H. T. Ali and S. Nazir, *Comput. Mater. Sci.*, 2025, **253**, 113880.
30 S. Shahzadi, I. M. Moussa, S. Mumtaz and S. Nazir, *RSC Adv.*, 2025, **15**, 17142–17152.
31 P. C. Rout and V. Srinivasan, *Phys. Rev. B*, 2019, **100**, 245136.
32 G. Guo, Y. Zhou, G. Guo and Z. Xie, *Mater. Today Chem.*, 2024, **35**, 101913.
33 M. Zafar, M. Muddassir, A. Ali, M. Shakil and I. H. El Azab, *Solid State Commun.*, 2025, **397**, 115825.
34 S. Ullah, J. Wang, P. Yang, L. Liu, J. Khan, S.-E. Yang, T. Xia, H. Guo and Y. Chen, *Sol. RRL*, 2021, **5**, 2000830.
35 G. Guo, S. Tan, G. Guo and Z. Xie, *Colloids Surf., A*, 2023, **659**, 130782.
36 G. Guo, C. Xu and P. Li, *Phys. Chem. Chem. Phys.*, 2025, **27**, 23091–23104.
37 G. Guo, Y. Chen, G. Guo and P. Li, *Sol. Energy*, 2026, **304**, 114203.
38 S. Al-Qaisi, H. Rached, T. A. Alrebdi, S. Bouzgarrou, D. Behera, S. K. Mukherjee, M. Khuili, M. Adam, A. S. Verma and M. Ezzeldien, *J. Comb. Chem.*, 2023, **44**, 2442–2452.
39 L. Yu and A. Zunger, *Phys. Rev. Lett.*, 2012, **108**, 068701.
40 G. J. Snyder and E. S. Toberer, *Nat. Mater.*, 2008, **7**, 105–114.
41 K. Schwarz, *J. Solid State Chem.*, 2003, **176**, 319–328.
42 P. Blaha, K. Schwarz, F. Tran, R. Laskowski, G. K. H. Madsen and L. D. Marks, *J. Chem. Phys.*, 2020, **152**, 074101.
43 J. Schmidt, C. L. Benavides-Riveros and M. A. Marques, *J. Phys. Chem. Lett.*, 2019, **10**, 6425–6431.
44 I. Jihad, M. H. S. Anfa, S. M. Alqahtani and F. H. Alharbi, *Comput. Mater. Sci.*, 2024, **244**, 113153.
45 J. P. Perdew, K. Burke and M. Ernzerhof, *Phys. Rev. Lett.*, 1996, **77**, 3865.
46 M. Derras, N. Hamdad, M. Derras and A. Gessoum, *Results Phys.*, 2013, **3**, 219–230.
47 S. Patil and S. Kaushik, *arXiv*, 2025, preprint, arXiv:2508.16219, DOI: 10.48550/arXiv.2508.16219.
48 X. Wu, D. Vanderbilt and D. Hamann, *Phys. Rev. B: Condens. Matter Mater. Phys.*, 2005, **72**, 035105.
49 S. Shang, Y. Wang and Z.-K. Liu, *Appl. Phys. Lett.*, 2007, **90**, 101909.
50 F. Mouhat and F.-X. Coudert, *Phys. Rev. B: Condens. Matter Mater. Phys.*, 2014, **90**, 224104.
51 U.-G. Jong, C.-J. Yu, J.-S. Ri, N.-H. Kim and G.-C. Ri, *Phys. Rev. B*, 2016, **94**, 125139.
52 A. Miyata, A. Mitioglu, P. Plochocka, O. Portugall, J. T.-W. Wang, S. D. Stranks, H. J. Snaith and R. J. Nicholas, *Nat. Phys.*, 2015, **11**, 582–587.
53 X. Zhou, J. Jankowska, H. Dong and O. V. Prezhdo, *J. Energy Chem.*, 2018, **27**, 637–649.
54 M.-W. Zeng, Y.-Q. Zhao and M.-Q. Cai, *Phys. Rev. Appl.*, 2021, **16**, 054019.
55 U. Rau, B. Blank, T. C. Müller and T. Kirchartz, *Phys. Rev. Appl.*, 2017, **7**, 044016.
56 M. Husain, N. Rahman, A. Azzouz-Rached, V. Tirth, H. Ullah, M. Elhadi, M. Uzair, A. Alotaibi, Q. Humayun, N. Sfina, *et al.*, *Silicon*, 2024, **16**, 2781–2790.
57 Z. Khadraoui, K. Horchani-Naifer, M. Ferhi and M. Ferid, *Chem. Phys.*, 2015, **457**, 37–42.
58 S. Horsley, M. Artoni and G. C. La Rocca, *Nat. Photon.*, 2015, **9**, 436–439.
59 N. Akhter, S. H. Alrefaee, A. Nurmuhammedov, M. Soliyeva, P. Ahmad, V. Tirth, A. Algahtani, Q. Mohsen, O. Alsaqer, N. Hadia, *et al.*, *Phys. Chem. Chem. Phys.*, 2025, **27**, 3160–3170.
60 M.-J. Choi, J.-W. Lee and H. W. Jang, *Adv. Mater.*, 2024, **36**, 2308827.
61 J. Wilcoxon, G. Samara and P. Provencio, *Phys. Rev. B: Condens. Matter Mater. Phys.*, 1999, **60**, 2704.
62 L. Yu and A. Zunger, *Phys. Rev. Lett.*, 2012, **108**, 068701.
63 M. Bilal, B. Khan, H. R. Aliabad, M. Maqbool, S. J. Asadabadi and I. Ahmad, *Comput. Phys. Commun.*, 2014, **185**, 1394–1398.
64 S. Walia, R. Weber, S. Balendhran, D. Yao, J. T. Abrahamson, S. Zhuiykov, M. Bhaskaran, S. Sriram, M. S. Strano and K. Kalantar-Zadeh, *Chem. Commun.*, 2012, **48**, 7462–7464.
65 D. Dalafave, *Mater. Chem. Phys.*, 2010, **119**, 195–200.
66 J. He, M. G. Kanatzidis and V. P. Dravid, *Mater. Today*, 2013, **16**, 166–176.
67 J. He and T. M. Tritt, *Science*, 2017, **357**, eaak9997.
68 H. E. Rebellon, O. F. P. Henao, E. I. Gutierrez-Velasquez, A. A. Amell and H. A. Colorado, *Eng. Sci.*, 2024, **29**, 1164.
69 M. H. Jeong, S. B. Kang and K. J. Choi, *ACS Appl. Electron. Mater.*, 2024, **6**, 2960–2968.
70 X.-M. Duan, G.-P. Chen, Y.-J. Shen, L.-H. Zheng and L.-B. Su, *Chin. Phys. Lett.*, 2019, **36**, 064201.
71 Y.-H. Pai, J. Tang, Y. Zhao and Z. Liang, *Adv. Energy Mater.*, 2023, **13**, 2202507.
72 G. K. Madsen and D. J. Singh, *Comput. Phys. Commun.*, 2006, **175**, 67–71.
73 S. Sundaram and E. Mazur, *Nat. Mater.*, 2002, **1**, 217–224.
74 M. Sajjad, Q. Mahmood, N. Singh and J. A. Larsson, *ACS Appl. Energy Mater.*, 2020, **3**, 11293–11299.
75 M. Y. Sofi, M. S. Khan and M. A. Khan, *Mater. Adv.*, 2024, **5**, 4913–4931.
76 J. Martin, T. Tritt and C. Uher, *J. Appl. Phys.*, 2010, **108**, 121101.
77 G. Qin, A. Huang, Y. Liu, H. Wang, Z. Qin, X. Jiang, J. Zhao, J. Hu and M. Hu, *Mater. Adv.*, 2022, **3**, 6826–6830.
78 O. L. Anderson, *J. Phys. Chem. Solids*, 1963, **24**, 909–917.
79 S. Daoud, *Int. J. Phys. Res.*, 2017, **5**, 7–10.
80 S.-B. Chen, S.-D. Guo, B. Lv and Y. S. Ang, *Phys. Rev. B: Condens. Matter Mater. Phys.*, 2024, **689**, 416201.
81 Y. Jain and R. Kurchania, *Mater. Sci. Semicond. Process.*, 2025, **186**, 109030.
82 M. Wolf, R. Hinterding and A. Feldhoff, *Entropy*, 2019, **21**, 1058.